Aminated silicon dioxide enriching iron-containing polyoxometalate catalyst confined in CdS for efficient H_2 evolution

Yinjuan Dong [a], Qiyu Hu [a], Bonan Li [a], Xiaohu Li [a], Mengxue Chen [a], Meiyu Zhang [a], Yu Feng [a], Yong Ding [a,b,*]

[a] *State Key Laboratory of Applied Organic Chemistry, Key Laboratory of Advanced Catalysis of Gansu Province, College of Chemistry and Chemical Engineering, Lanzhou University, Lanzhou 730000, China*
[b] *State Key Laboratory for Oxo Synthesis and Selective Oxidation, Lanzhou Institute of Chemical Physics Chinese Academy of Sciences, Lanzhou 730000, China*

ARTICLE INFO

ABSTRACT

The rational design of an artificial system that mimics natural photosynthesis for H_2 evolution remains a substantial yet engaging challenge. Efficient light absorption, charge separation and associated surface reactions are crucial aspects of semiconductor photocatalytic system for efficient water splitting. Herein, a catalyst assembly of p-SiO$_2$-NH$_3$-Fe$_{11}$POM@CdS was constructed by partially etched SiO$_2$-NH$_2$ coating CdS (p-SiO$_2$-NH$_2$@CdS) bound iron-based polyoxometalate (Fe$_{11}$POM) in the interstitial space. In the hybrid catalyst, Fe$_{11}$POM acts as catalyst and p-SiO$_2$-NH$_2$@CdS as light-harvesting material as well as Fe$_{11}$POM enrichment center, respectively. The p-SiO$_2$-NH$_3$-Fe$_{11}$POM@CdS catalyst exhibits a high H_2 evolution activity of 23.1 mmol g^{-1} h^{-1} with turnover number (TON) of 3225 and apparent quantum efficiency (AQE) of 71% under 420 nm LED illumination. The electrons transfer from p-SiO$_2$-NH$_2$@CdS to Fe$_{11}$POM, affording electrons accumulated in Fe$_{11}$POM for H_2 evolution. Our strategy of building hybrid photocatalyst will provide a new way to construct efficient catalyst assembly for water splitting.

1. Introduction

Developing efficient photochemical conversion technologies are of great importance for alternative clean energy supplies [1,2]. As a renewable and clean energy source with high energy density of 142 MJ kg^{-1}, hydrogen (H_2) plays an increasingly significant role in reducing humanity's dependence on fossil fuel [3–5]. In the past few decades, substantial remarkable photocatalysts have been developed for heterogeneous [6–10] and homogeneous [11–15] H_2 evolution. Homogeneous catalyst with metal-atom economy, readily characterized with clear structure, identifiable active site and clear catalytic mechanism allow finely structural regulation to acquire high intrinsic activity. However, it is hard to recover a homogeneous catalyst from the reaction solution and meet stability challenge [16]. In contrast, heterogeneous catalyst is stable and convenient for recycling from the reaction mixtures. Unfortunately, it is still intrinsically plagued by surface heterogeneity and structural complexity, which makes it difficult to clarify the catalytic mechanism [17]. Therefore, a promising photocatalyst should integrate the advantages of homogenous and heterogeneous catalyst to realize "homogenous in heterogeneous catalysis".

Recently, heterogeneous semiconductor photocatalysts (such as CdS [18–20], g-C$_3$N$_4$ [21–24], TiO$_2$ [25–27] and BiVO$_4$ [28–30]) incorporating both light harvesting material and catalysis have been considered as a feasible and prospective means of photocatalytic water splitting. CdS is a great potential semiconductor photocatalyst for light-driven H_2 evolution because of its relatively narrow band-gap (E_g = 2.4 eV) and proper conduction band position [18,31]. However, H_2 evolution rate of pure CdS is seriously limited by the rapid recombination of photogenerated carriers and poor stability under irradiation [32]. To solve these problems, many approaches have been proposed, such as impurity doping, surface sensitization, construction of heterojunction and introduction of cocatalyst [20,31–36]. The heterogenization of homogenous catalyst is a promising strategy to realize the recovery and enhancement of stability for homogeneous catalyst. Krauss et al. used CdSe capped with dihydrolipoic acid as light-harvesting material in combination with a soluble Ni^{2+}-DHLA catalyst for enhancing H_2 evolution [37]. Kong

---

et al. presented a strategy for enhanced H_2 evolution by integrating with $Ln_{52}Ni_{56}$ clusters onto CdS surface [38]. Nevertheless, organic ligands of the complex molecule are prone to be oxidized, and hydrolyzed with their active transition metal centers, leading to the formation of colloidal metal oxides.

As a huge class of unique metal-oxo cluster with well-defined structure and nanosize, polyoxometalates (POMs) perform multi-electron reduction and oxidation property and give excellent H_2- or/and O_2- evolution [39–43]. Traditionally, photocatalytic water splitting system with the presence of POMs follows the three-component of "photosensitizer-catalyst-sacrificial agent" [44–49]. Although important advances have been gained in POM-based photocatalytic H_2 evolution, it is a challenge to design "catalyst and light harvesting material assembly" combining POMs and semiconductor together, which can simulate the photosystem I of the nature and then facilitate electron transfer to realize efficient photocatalytic H_2 evolution.

In this work, a hybrid p-SiO_2-NH_3-$Fe_{11}POM@CdS$ catalyst assembly was constructed to implant the iron-based polyoxometalate ($Fe_{11}POM$) in the interstitial space of the partially etched SiO_2-NH_2 coated with CdS (p-SiO_2-$NH_2@CdS$) through the electrostatic interaction between the anionic $Fe_{11}POM$ and the cationic p-SiO_2-$NH_2@CdS$ fragment. The integrated, abundant-element-based hybrid catalyst functions as an good photocatalytic system for water splitting, in which shows durable, highly efficient and recyclable performance for this hybrid catalyst.

2. Experimental

2.1. Synthesis of $Na_{27}[Fe_{11}(H_2O)_{14}(OH)_2(W_3O_{10})_2(\alpha\text{-}SbW_9O_{33})_6]$

$Na_{27}[Fe_{11}(H_2O)_{14}(OH)_2(W_3O_{10})_2(\alpha\text{-}SbW_9O_{33})_6]$($Fe_{11}POM$ for clarity) was prepared according to the literature procedure [42]. Distilled water (80 mL) containing as-prepared SbW_9 (9.45 g, 3.3 mmol) (In supporting information) and $FeCl_3$ (1.16 g, 7.2 mmol) was added in a beaker, and the pH was 3.0 after 20 min of ultrasonication. The mixture was stirred for 1 h at 90 °C, and the precipitate was removed by filtration. Slowly evaporate of the filtrate at room temperature for one week, obtaining yellow $Fe_{11}POM$ crystals. Elemental analysis for $Fe_{11}POM$: calcd. For Na, 3.23; Fe, 3.14; Sb, 3.92; W, 59.2%; found for Na, 3.25; Fe, 3.11; Sb, 3.85; W, 58.8%.

2.2. Synthesis of p-SiO_2-$NH_2@CdS$

p-SiO_2-$NH_2@CdS$ was prepared as following: Firstly, the SiO_2 template was synthesized according to Stöber's method [50]. Typically, aqueous ammonia (3.1 g, 32 wt%) and 10 mL of deionized water were added to 58.5 g of ethanol. After stirring for 30 min, tetraethoxysilane (TEOS, 5.6 mL) was added to the above solution under vigorous stirring and left stationary for 1 h to yield silica spheres. After washing three times with ethanol by centrifugation, the particles were transferred to a mixture of isopropanol (50 g) and 3-aminopropyl-triethoxysilane (APTES, 3 g) and heated to 80 °C for 2 h. The product of -NH_2 functionalized silica (SiO_2-NH_2) was obtained.

Secondly, 0.25 g of SiO_2-NH_2 powder was dispersed in 10 mL distilled water. After 30 min of ultrasonication, a solution of Cd $(NO_3)_2 \cdot 4H_2O$ (0.5 g), $CS(NH_2)_2$ (0.37 g) and ethylenediamine (20 mL) was added to above solution. Stirring for 1 h, the resulting homogenous mixture was transferred into an 80 mL teflon-lined stainless steel autoclave and heated at 180 °C for 24 h. Cooling down to room temperature, the product of SiO_2-$NH_2@CdS$ was collected by centrifugation, washing with ethanol, and drying at 60 °C. Finally, 0.5 g of SiO_2-$NH_2@CdS$ was treated with 2.5 M NaOH solution at 90 °C for 4 h, then centrifuged and washed three times with distilled water. A yellow product of partially etched SiO_2-NH_2 coated with CdS was prepared (p-SiO_2-$NH_2@CdS$).

2.3. Synthesis of p-SiO_2-NH_3-$Fe_{11}POM@CdS$ catalyst

The composite material of p-SiO_2-NH_3-$Fe_{11}POM@CdS$ was obtained via impregnation method. Specially, 10 mg of $Fe_{11}POM$ were mixed with 10, 30, 50, 70 and 90 mg of p-SiO_2-$NH_2@CdS$ in 10 mL distilled water, respectively. The pH was adjusted to 3 by 1 M HCl (~5 drips) and then stirred at 35 °C for 12 h. Then p-SiO_2-NH_3-$Fe_{11}POM@CdS$ composite was obtained by centrifugation and dried at 60 °C.

Besides, p-SiO_2-NH_3-$Fe_{11}POM@CdS$ (Cd:Si=2:1), p-SiO_2-NH_3-$Fe_{11}POM@CdS$ (Cd:Si=1:1), p-SiO_2-NH_3-$Fe_{11}POM@CdS$ (Cd:Si=1:2) composites were also prepared with the similar procedure using different mass ratios of Cd precursor ($Cd(NO_3)_2 \cdot 4H_2O$) and Si precursor (SiO_2-NH_2) at 2:1, 1:1, 1:2, respectively.

2.4. Photocatalytic H_2 evolution

Photocatalytic tests were performed as following: the optimal mass of catalyst (3 mg) was dispersed in 15 mL of an aqueous solution containing 10 vol% lactic acid as sacrificial reagent in a quartz cell. The above solution was deaerated by purging with Ar gas in a flask (33.6 mL) sealed with a rubber septum for 50 min (the volume of the reaction solution was 15 mL). The reaction was then initiated by irradiating the solution using a LED light (100 mW cm^{-2}, λ = 420 nm). After each irradiation, 150 μL Ar was injected into the flask and then the same volume of gas in the headspace of the flask was withdrawn using a SGE gas-tight syringe. The amount of H_2 was determined by GC. For stability testing, once the photocatalytic reaction in the 3 h cycle was completed, the reactor was degassed in vacuum before starting the subsequent cycles.

2.5. Photoelectrochemical measurement

The electrochemical impedance spectra and photocurrent response of as-prepared samples were detected on a CHI 760D workstation (CH Instruments Co.) with a three-electrode setup under simulated solar light irradiation (AM 1.5 G filter, 100 mW cm^{-2}, 300 W Xe lamp, Perfect Light). The fabricated photoanode, carbon rod and Ag/AgCl electrode were conducted as working electrode, counter electrode and reference electrode, respectively.

2.6. Tengs blue color reaction

To confirm the formation of Fe^{2+} intermediate species over p-SiO_2-NH_3-$Fe_{11}POM@CdS$ under LED light irradiation (100 mW cm^{-2}, λ = 420 nm), the following experiments were carried out. The system containing 5 mg of p-SiO_2-NH_3-$Fe_{11}POM@CdS$ and 10 mL of deionized water was degassed with Ar for 0.5 h. Then, the system was exposed to LED light irradiation for 3 h. The produced Fe^{2+} intermediate species of reaction solution can be detected by $K_3[Fe(CN)_6]$ with a blue-green precipitate $KFe[Fe(CN)_6]$.

3. Results and discussion

3.1. Characterization of catalyst

$Fe_{11}POM$ is constituted by six trilacunary $[\alpha\text{-}SbW_9O_{33}]^{9-}$ fragments linked by electrophilic $[Fe_{11}(H_2O)_{14}(OH)_2(W_3O_{10})_2]^{27+}$ cluster units and is characterized by elemental analysis and FT-IR (see synthesis of $Fe_{11}POM$ and Fig. S1) [42]. The UV–vis absorption spectra of $Fe_{11}POM$ testify hydrolytically stable in our reaction condition since it remains unchanged for aging 10 h in aqueous solution containing 10 vol% lactic acid (Fig. S2). A schematic view of p-SiO_2-NH_3-$Fe_{11}POM@CdS$ preparation is shown in Fig. 1. Firstly, the functionalization the silica surface with -NH_2 groups (SiO_2-NH_2) was obtained. Subsequently, SiO_2-NH_2 was coated with CdS via hydrothermal method, generating SiO_2-$NH_2@CdS$ sample. Whereafter, the SiO_2 as sacrificial template was
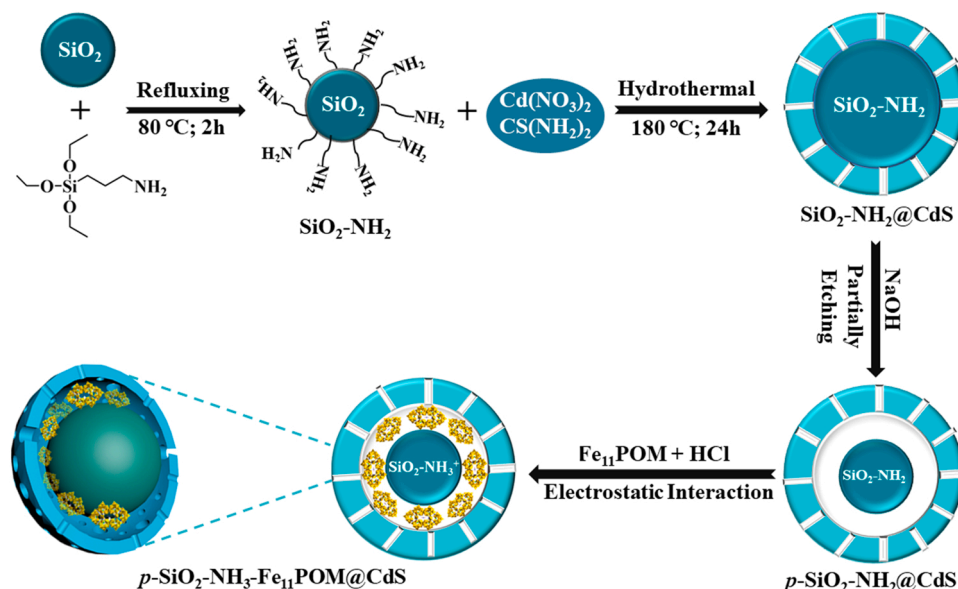
Fig. 1. Schematic illustration for the formation process over p-SiO$_2$-NH$_3$-Fe$_{11}$POM@CdS photocatalyst.

partially etched by using 2.5 M NaOH, resulting in p-SiO$_2$-NH$_2$@CdS sample with interstitial space. Finally, Fe$_{11}$POM molecular spontaneously and irreversibly enters into the interstitial space of p-SiO$_2$-NH$_2$@CdS in the acidic condition via electrostatic interaction.

The negatively charged Fe$_{11}$POM is entering into the positively charged p-SiO$_2$-NH$_2$@CdS interstitial space through three processes: (i) p-SiO$_2$-NH$_2$@CdS is converted as p-SiO$_2$-NH$_3^+$@CdS with HCl (~5 drops) by acidizing process (p-SiO$_2$-NH$_2$@CdS + H$^+$ → p-SiO$_2$-NH$_3^+$@CdS); (ii) Electrostatic force-driven encapsulation of anionic Fe$_{11}$POM into the acidulated p-SiO$_2$-NH$_2$@CdS interstitial space to form p-SiO$_2$-NH$_3^+$@CdS/Fe$_{11}$POM; (iii) The target p-SiO$_2$-NH$_3$-Fe$_{11}$POM@CdS composite catalyst was obtained after washing by water to remove nonencapsulated Fe$_{11}$POM and potassium cations.

The positive zeta potential values (ζ, 0 ~ 25 mV) are associated with acidulated p-SiO$_2$-NH$_2$@CdS, while negative zeta potential values (ζ, −75 ~ −25 mV) are observed over Fe$_{11}$POM (Fig. 2a). Meanwhile, to examine the charge property of acidulated p-SiO$_2$-NH$_2$@CdS, a cationic dye methylene blue (MB$^+$) and an anionic dye methyl orange (MO$^-$) were used for ion-exchange experiments (Fig. S3). The results show that anionic MO$^-$ is easily exchanged into acidulated p-SiO$_2$-NH$_2$@CdS, while anionic MB$^+$ couldn't be exchanged into acidulated p-SiO$_2$-NH$_2$@CdS, confirming that acidulated p-SiO$_2$-NH$_2$@CdS is positively charged. Therefore, the hybrid photocatalyst p-SiO$_2$-NH$_3$-Fe$_{11}$POM@CdS was obtained via electrostatic interaction between two oppositely charged components, confirming acidulated p-SiO$_2$-NH$_2$@CdS is the enrichment center for Fe$_{11}$POM.

As shown in Fig. 2b-c, the specific surface area (BET) and total pore volume (V_t) of the p-SiO$_2$-NH$_2$@CdS sample are 35.7 m^2 g^{-1} and 0.09 cm^3 g^{-1}, respectively, which are larger than those of p-SiO$_2$-NH$_3$-Fe$_{11}$POM@CdS (14.9 m^{2}g^{-1} and 0.07 cm^3 g^{-1}). Introduction of Fe$_{11}$POM anion into the interstitial space of p-SiO$_2$-NH$_2$@CdS induces a decrease of BET and V_t. The close integration between Fe$_{11}$POM and the size of p-SiO$_2$-NH$_2$@CdS interstitial space indicates that the dissolved Fe$_{11}$POM upon entry, providing an additional entropic driving force for encapsulation.

Scanning electron microscopy (SEM) in Fig. 2d shows that p-SiO$_2$-NH$_3$-Fe$_{11}$POM@CdS catalyst is spherical. Transmission electron microscope (TEM) and high-resolution transmission electron microscopy (HRTEM) images for p-SiO$_2$-NH$_3$-Fe$_{11}$POM@CdS are shown in Fig. 2e-f and Fig. S4. The boundary between CdS and p-SiO$_2$-NH$_3$-Fe$_{11}$POM in TEM (Fig. 2e) is marked with red dotted lines. The inside section of the hybrid catalyst is p-SiO$_2$-NH$_3$-Fe$_{11}$POM and the outer light black section

is CdS. The HRTEM of p-SiO$_2$-NH$_3$-Fe$_{11}$POM@CdS (Fig. 2f) reveals fringe spacing of about 0.336 indexing to the CdS (002) lattice planes. EDS spectrum (Fig. S5) shows Fe, Sb, W, Cd, S, N, Si and O element signals, and EDS analysis result is listed in Table S1. The corresponding element mappings (Fig. 2g) reveal the homogeneous distribution of the various elements in the p-SiO$_2$-NH$_2$ @CdS (Cd, S, N, Si and O) and Fe$_{11}$POM (Fe, Sb, W and O).

The IR spectra of p-SiO$_2$-NH$_2$@CdS, Fe$_{11}$POM and p-SiO$_2$-NH$_3$-Fe$_{11}$POM@CdS are shown in Fig. 3a. Apart from peaks attribute to p-SiO$_2$-NH$_2$@CdS, and p-SiO$_2$-NH$_3$-Fe$_{11}$POM@CdS also exhibits a series of bands of Fe$_{11}$POM with terminal W=O stretching (937 cm^{-1}) and W-O-W bending (892 and 785 cm^{-1}). In the high-frequency region, the broad and intense bands at 3490–3380 cm^{-1} are ascribed to the O-H stretching vibrations of lattice or coordination water molecules. From Fig. 3b, the peaks centered at 2849 and 2916 cm^{-1} with N-H stretching vibration appear in p-SiO$_2$-NH$_2$@CdS and p-SiO$_2$-NH$_3$-Fe$_{11}$POM@CdS samples, while no signal exists in Fe$_{11}$POM. For p-SiO$_2$-NH$_3$-Fe$_{11}$POM@CdS photocatalyst, the new bands located at 832, 845 and 856 cm^{-1} are assigned to Fe-N oscillator, suggesting that p-SiO$_2$-NH$_2$@CdS and Fe$_{11}$POM active species are successfully combined together.

The UV–vis spectra of Fe$_{11}$POM, p-SiO$_2$-NH$_2$@CdS and p-SiO$_2$-NH$_3$-Fe$_{11}$POM@CdS are displayed in Fig. S7. The observed characteristic absorption band at 504 nm suggests the presence of the first excitation (1 S) peak in p-SiO$_2$-NH$_2$@CdS. For p-SiO$_2$-NH$_3$-Fe$_{11}$POM@CdS hybrid photocatalyst, an obviously enhanced absorbance appears at 501 nm (excitation band) and the characteristic absorbance is at 272 nm. A slight blue shift of p-SiO$_2$-NH$_3$-Fe$_{11}$POM@CdS is observed compared with that of p-SiO$_2$-NH$_2$@CdS (504 nm) and Fe$_{11}$POM (268 nm).

X-ray photoelectron spectroscopy (XPS) analysis was performed to gain a deep understanding of surface composition of the catalyst. As expected, seven peaks of Cd, S, N, Fe, Sb, W and O are clearly observed (Fig. S8). The valence state of Fe was studied by XANES measurement (Fig. 3c). From XANES, Fe$_{11}$POM and p-SiO$_2$-NH$_3$-Fe$_{11}$POM@CdS have similar absorption edge with those of Fe$_2$O$_3$ and FeCl$_3$, meaning that the valence state of Fe in Fe$_{11}$POM and p-SiO$_2$-NH$_3$-Fe$_{11}$POM@CdS are + 3. For p-SiO$_2$-NH$_3$-Fe$_{11}$POM@CdS XPS tests, two deconvolution peaks of Fe 2p region at 723.2 eV (Fe 2p$_{1/2}$) and 711.7 eV (Fe 2p$_{3/2}$), along with two peaks of W 4 f region at 37.8 eV (W 4 f$_{5/2}$) and 35.7 eV (W 4 f$_{7/2}$), are certified as characteristic peaks of Fe$_{11}$POM (Fig. S9 and Fig. 3d). The weak signals of Fe peaks in high resolution XPS spectrum are due to Fe$_{11}$POM in the interstitial space of p-SiO$_2$-NH$_2$@CdS and its minuscule content. The loading amounts of Fe (0.12%), Sb (0.18%) and W (1.88%)

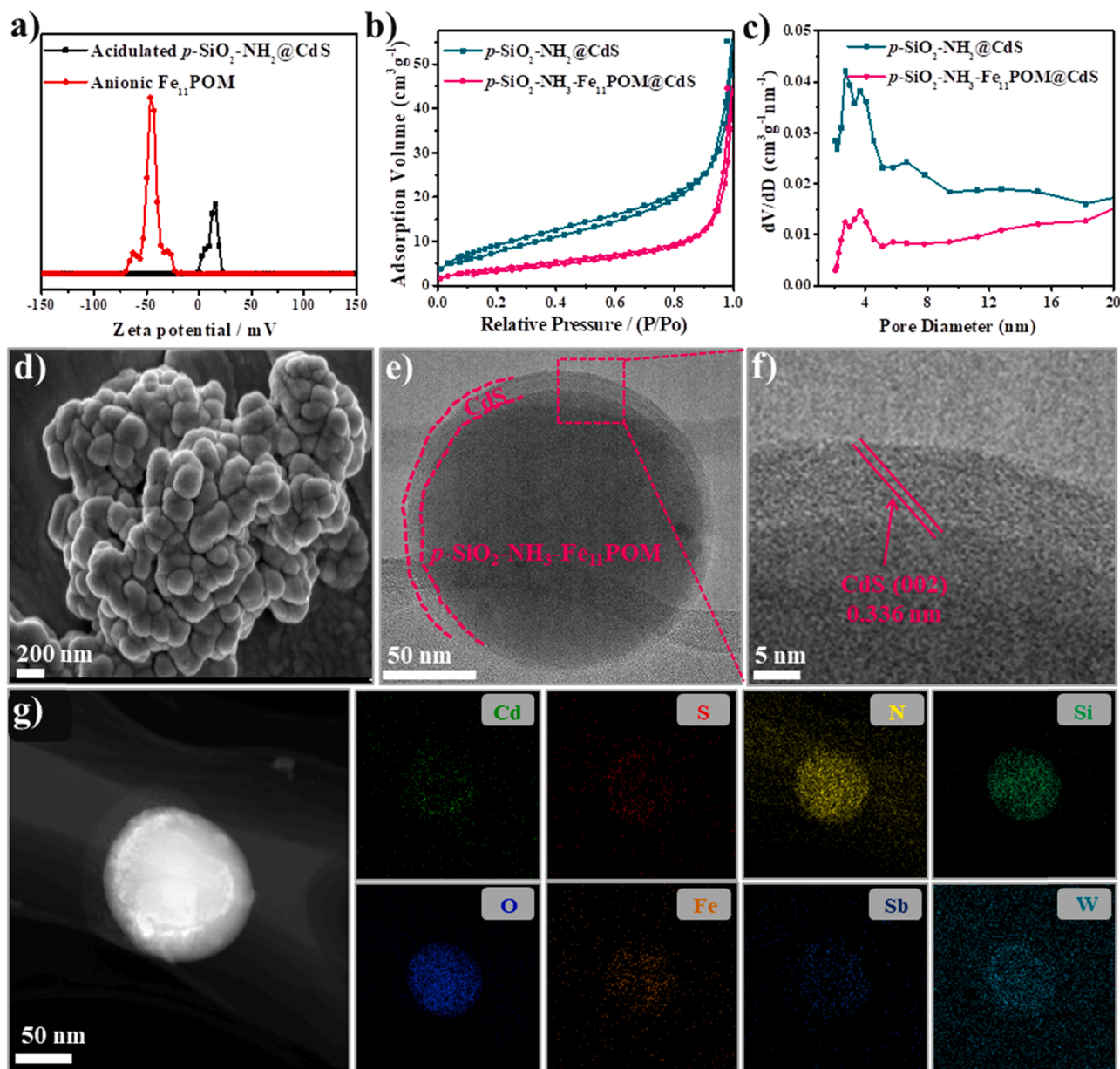**Fig. 2.** (a) Zeta potential distribution of acidulated *p*-SiO$_2$-NH$_2$@CdS and Fe$_{11}$POM. (b) The N$_2$ adsorption–desorption isotherms, and (c) pore size distributions of *p*-SiO$_2$-NH$_2$@CdS and *p*-SiO$_2$-NH$_3$-Fe$_{11}$POM@CdS. (d) SEM image of *p*-SiO$_2$-NH$_3$-Fe$_{11}$POM@CdS. (e) TEM image of *p*-SiO$_2$-NH$_3$-Fe$_{11}$POM@CdS and (f) HRTEM image from magnified red rectangle of (e). (g) EDX mapping of the various elements contained in the *p*-SiO$_2$-NH$_2$@CdS and Fe$_{11}$POM.

are quantified by inductively coupled plasma atomic emission spectrometry (ICP-AES), in which experimental molar ratio confirms with the theoretical ratio of Fe$_{11}$POM, indicating the Fe$_{11}$POM molecule keeps intact in the *p*-SiO$_2$-NH$_3$-Fe$_{11}$POM@CdS catalyst.

For *p*-SiO$_2$-NH$_3$-Fe$_{11}$POM@CdS composite, the high resolution Cd 3d XPS spectra (Fig. 3e) show two peaks at 412.1 and 405.3 eV corresponding to the binding energy of Cd 3d$_{3/2}$ and Cd 3d$_{5/2}$, respectively. The S 2p XPS spectra (Fig. 3f) are divided into S 2p$_{1/2}$ (162.8 eV) and S 2p$_{3/2}$ (161.7 eV). The N 1 s XPS spectra (Fig. S10) show carbon−amine bonds (C−N, 399.7 eV) and amide bonds (N − C(O), 400.8 eV). The positively shift of binding energy of Cd 3d, S 2p and N 1 s over *p*-SiO$_2$-NH$_3$-Fe$_{11}$POM@CdS represents a kind of electron donor state [51], revealing the electron transfer direction is from *p*-SiO$_2$-NH$_2$@CdS to Fe$_{11}$POM.

3.2. Photocatalytic hydrogen evolution

As the optical property of a catalyst is a key parameter in determining the photocatalytic activity, UV–vis diffuse reflectance was conducted to investigate the photoabsorption property of the as-prepared samples [52] (Fig. 4a). *p*-SiO$_2$-NH$_2$@CdS absorbs light from the UV to the visible region, while Fe$_{11}$POM shows very weak absorbance, indicating that *p*-SiO$_2$-NH$_2$@CdS takes the responsibility of the light harvester in *p*-SiO$_2$-NH$_3$-Fe$_{11}$POM@CdS hybrid catalyst under visible light irradiation. The *p*-SiO$_2$-NH$_3$-Fe$_{11}$POM@CdS composite exhibits the similar optical absorbance with *p*-SiO$_2$-NH$_2$@CdS. Tauc plots are explored to assess the band gap energies of Fe$_{11}$POM and *p*-SiO$_2$-NH$_2$@CdS (Fig. S11). The values of the bandgap energy of *p*-SiO$_2$-NH$_2$@CdS and Fe$_{11}$POM are 1.95 eV and 2.29 eV, respectively, through extrapolating the linear region of the absorbance squared versus energy.

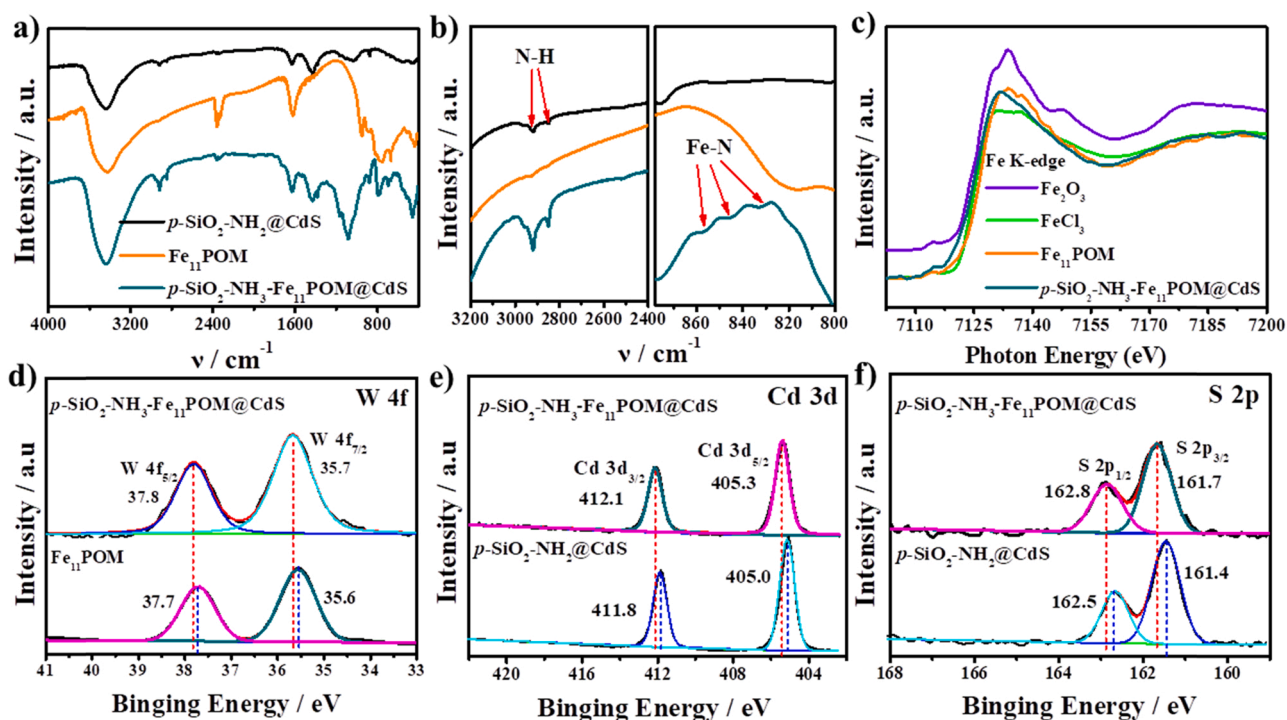Mott-Schottky plot is used to evaluate the conductivity types [18,53]

Fig. 3. (a) FT-IR spectra of *p*-SiO$_2$-NH$_2$@CdS, Fe$_{11}$POM and *p*-SiO$_2$-NH$_3$-Fe$_{11}$POM@CdS. (b) Magnified FT-IR spectra toward N-H stretching vibration and Fe-N oscillator. (c) XANES spectra at Fe K-edge of samples. (d) High-resolution XPS spectra of W 4 f for Fe$_{11}$POM and *p*-SiO$_2$-NH$_3$-Fe$_{11}$POM@CdS composite. High-resolution XPS spectra of Cd 3d (e) and S 2p (f) for *p*-SiO$_2$-NH$_2$@CdS and *p*-SiO$_2$-NH$_3$-Fe$_{11}$POM@CdS.
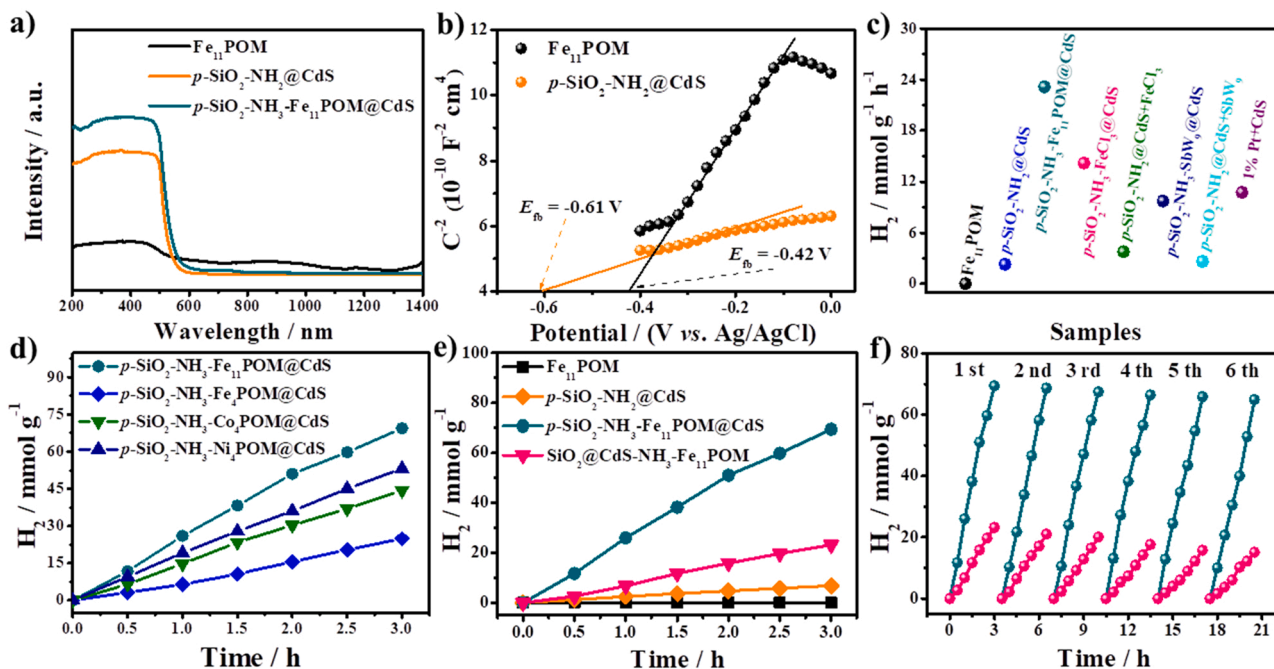

Fig. 4. (a) UV–vis diffuse reflectance spectrum measurements and (b) Mott-Schottky plots. (c) A comparison of H$_2$ evolution rate for reference samples. (d) A comparison of the time course of photocatalytic H$_2$ evolution activity of different *p*-SiO$_2$-NH$_3$-POMs@CdS. (e) Time course of H$_2$ evolution over Fe$_{11}$POM, *p*-SiO$_2$-NH$_2$@CdS, *p*-SiO$_2$-NH$_3$-Fe$_{11}$POM@CdS and SiO$_2$@CdS-NH$_3$-Fe$_{11}$POM. (f) Durability testing for the photocatalytic water splitting performance of *p*-SiO$_2$-NH$_3$-Fe$_{11}$POM@CdS (cyan line) and SiO$_2$@CdS-NH$_3$-Fe$_{11}$POM (red line) under the same catalytic conditions for six times. Reaction conditions: 3 mg of sample, 15 mL of aqueous lactic acid solution (10%, v/v), illumination with 420 nm LED lamp (100 mW cm^{-2}).

of *p*-SiO$_2$-NH$_2$@CdS and Fe$_{11}$POM with a three-electrode system at frequency 1.0 kHz (Fig. 4b). The positive slopes of C^{-2}–E plots conform to n-type semiconductors of *p*-SiO$_2$-NH$_2$@CdS and Fe$_{11}$POM. The flat-band potentials (E_{fb}) of Fe$_{11}$POM and *p*-SiO$_2$-NH$_2$@CdS are − 0.42 V and

− 0.61 V vs. Ag/AgCl, respectively. Accordingly, the conduction band (CB) potentials for Fe$_{11}$POM and *p*-SiO$_2$-NH$_2$@CdS are − 0.62 eV and − 0.81 eV, which are − 0.42 V and − 0.61 V vs. normal hydrogen electrode (NHE) ($E_{NHE}= E_{Ag/AgCl}+ E^{\theta}_{Ag/AgCl}$; $E^{\theta}_{Ag/AgCl}$=0.1976 V) [54].

Furthermore, combining the bandgap energy and Mott-Schottky results, the valence band (VB) potentials are calculated as 1.68 and 1.92 eV ($E_{VB}= E_{CB}+ E_g$; vs. NHE) [55] for p-SiO$_2$-NH$_2$@CdS and Fe$_{11}$POM, respectively. The energy band position diagram in Fig. S12 demonstrates the electron transfer direction is from p-SiO$_2$-NH$_2$@CdS to Fe$_{11}$POM.

The photocatlytic H$_2$ evolution was investigated over as-prepared catalysts using lactic acid as sacrificial reagent under visible light irradiation (λ = 420 nm) (Fig. S13). The rate of Cd(NO$_3$)$_2$/SiO$_2$-NH$_2$ and suitable amount of Fe$_{11}$POM are two pre-requisites for obtaining good H$_2$ evolution activity of p-SiO$_2$-NH$_3$-Fe$_{11}$POM@CdS. The influence of the ratio of Cd(NO$_3$)$_2$ and SiO$_2$-NH$_2$ by fixing the mass of Fe$_{11}$POM (20%) was explored (Fig. S14a), and the varying ratios of Cd(NO$_3$)$_2$/SiO$_2$-NH$_2$ are 2:1, 1:1 and 1:2. When the ratios of Cd(NO$_3$)$_2$/SiO$_2$-NH$_2$ are 1:1, p-SiO$_2$-NH$_3$-Fe$_{11}$POM@CdS exhibits the best performance with H$_2$ evolution amount of 69.4 mmol g^{-1}. The effect of Fe$_{11}$POM amounts in p-SiO$_2$-NH$_3$-Fe$_{11}$POM@CdS composite over the H$_2$ evolution activities is investigated in Fig. S14b. With the increase of Fe$_{11}$POM, the H$_2$ evolution activity of p-SiO$_2$-NH$_3$-Fe$_{11}$POM@CdS increases. When the addition amount of Fe$_{11}$POM continues to increase, the activity of H$_2$ evolution basically remains unchanged. This suggests that well-balanced Fe$_{11}$POM content improves the catalytic performance of p-SiO$_2$-NH$_3$-Fe$_{11}$POM@CdS.

It is essential to optimize the amount of catalyst for the H$_2$ evolution activity since it will affect the dispersity, the contact of catalyst with reaction solution (sacrificial agent/water molecules) and the capacity of light absorption. Photocatalytic H$_2$ evolution was examined under different amount of p-SiO$_2$-NH$_3$-Fe$_{11}$POM@CdS (Fig. S15). The maximum amount of H$_2$ evolution was obtained when the amount of p-SiO$_2$-NH$_3$-Fe$_{11}$POM@CdS is 3 mg. A decreased activity for H$_2$ evolution was observed when larger amount of p-SiO$_2$-NH$_3$-Fe$_{11}$POM@CdS (> 3 mg) was used. Therefore, the appropriate 3 mg amount of p-SiO$_2$-NH$_3$-Fe$_{11}$POM@CdS hybrid catatlyst is selected for further optimization of the H$_2$ evolution.

The SiO$_2$ template does not contribute catalytic activity since the H$_2$ amount over SiO$_2$, SiO$_2$-NH$_2$ is below detection limit (Fig. S16). Under appropriate conditions, p-SiO$_2$-NH$_3$-Fe$_{11}$POM@CdS exhibits the highest catalytic activity with a high H$_2$ evolution rate of 23.1 mmol g^{-1} h^{-1}, TON of 3225 and apparent quantum efficiency (AQE) 71% at 420 nm under 3 h irradiation. Control experiments about H$_2$ evolution performance to clarify the effect of p-SiO$_2$-NH$_2$@CdS and Fe$_{11}$POM were conducted (Fig. 4c and Fig. S17) over the pristine CdS, p-SiO$_2$-NH$_2$@CdS, Fe$_{11}$POM and physical mixture samples (such as CdS+Fe$_{11}$POM and p-SiO$_2$-NH$_2$@CdS+Fe$_{11}$POM). A relatively low H$_2$ evolution of Fe$_{11}$POM (0.1 mmol g^{-1}) is observed. The catalyst assembly of p-SiO$_2$-NH$_3$-Fe$_{11}$POM@CdS brings obvious enhancement of photocatalytic H$_2$ evolution compared with the above other samples.

Additionally, the H$_2$ evolution rate of p-SiO$_2$-NH$_3$-Fe$_{11}$POM@CdS hybrid catalyst is 10.1, 1.6 and 2.4 times as high as those of p-SiO$_2$-NH$_2$@CdS, p-SiO$_2$-NH$_3$-SbW$_9$@CdS and p-SiO$_2$-NH$_3$-FeCl$_3$@CdS, respectively, and even exceeds that of 1%Pt+CdS. Noticeably, activities of p-SiO$_2$-NH$_3$-Fe$_{11}$POM@CdS, p-SiO$_2$-NH$_3$-SbW$_9$@CdS and p-SiO$_2$-NH$_3$-FeCl$_3$@CdS composites are all higher than the physical mixing samples of p-SiO$_2$-NH$_2$@CdS+Fe$_{11}$POM, p-SiO$_2$-NH$_2$@CdS+SbW$_9$ and p-SiO$_2$-NH$_2$@CdS+FeCl$_3$, accordingly. The structure of catalyst is significant for enhancing its activity since it efficiently facilitates charge separation and adequately exerts the effect of catalyst.

More significantly, the template synthesis of p-SiO$_2$-NH$_3$-Fe$_{11}$POM@CdS is facilely extended to the fabrication of other p-SiO$_2$-NH$_3$-POMs@CdS catalysts with different POM including p-SiO$_2$-NH$_3$-Fe$_4$POM@CdS, p-SiO$_2$-NH$_3$-Co$_4$POM@CdS and p-SiO$_2$-NH$_3$-Ni$_4$POM@CdS. The detailed IR characterizations over different POMs have also been executed (Fig. S18-20). As shown in Fig. 4d, the H$_2$ evolution amounts of p-SiO$_2$-NH$_3$-Fe$_{11}$POM@CdS (69.4 mmol g^{-1}), p-SiO$_2$-NH$_3$-Ni$_4$POM@CdS (53.1 mmol g^{-1}), p-SiO$_2$-NH$_3$-Co$_4$POM@CdS (44.4 mmol g^{-1}) and p-SiO$_2$-NH$_3$-Fe$_4$POM@CdS (24.9 mmol g^{-1}), are 10.1, 7.7, 6.4 and 3.6 times than that of p-SiO$_2$-NH$_2$@CdS

(6.9 mmol g^{-1}), respectively. This synthetic strategy offers a general method to prepare of the novel "two-in-one" p-SiO$_2$-NH$_3$-POMs@CdS composite with the combination of catalyst and light harvesting material.

The structure of catalyst determination its catalytic performance is a universal principle. For comparison, SiO$_2$@CdS-NH$_3$-Fe$_{11}$POM was prepared as a reference sample, which Fe$_{11}$POM was bound in SiO$_2$@CdS-NH$_2$ solid exterior shell. And the detailed characterizations of TEM, FT-IR and XRD for SiO$_2$@CdS-NH$_3$-Fe$_{11}$POM was executed (Fig. S21). As shown in Fig. 4e, compared with p-SiO$_2$-NH$_3$-Fe$_{11}$POM@CdS hybrid catalyst, the sample of SiO$_2$@CdS-NH$_3$-Fe$_{11}$POM exhibits an obvious decrease activity in H$_2$ evolution (69.4 vs. 23.2 mmol g^{-1}). The construction of p-SiO$_2$-NH$_3$-Fe$_{11}$POM@CdS through introducing Fe$_{11}$POM catalysts into p-SiO$_2$-NH$_2$@CdS interstitial space speeds up the spatially separated charges. Whereas for SiO$_2$@CdS-NH$_3$-Fe$_{11}$POM catalyst, Fe$_{11}$POM adsorbed on the outer surface of SiO$_2$@CdS-NH$_2$ blocks light, thus leading to a decrease in photocatalytic H$_2$ evolution. The stabilities of two catalysts were tested for photocatalytic H$_2$ evolution (Fig. 4f and Fig. S22). It is found that both of samples demonstrate excellent cycling stability, which is sustainable for at least six of cycles with little activity fading. The H$_2$ evolution activity of p-SiO$_2$-NH$_3$-Fe$_{11}$POM@CdS generates slight reduction after six cycles since the CdS photocorrosion. Additionally, all the XRD diffraction peaks in Fig. S23 of the recovered p-SiO$_2$-NH$_3$-Fe$_{11}$POM@CdS are consistent with the fresh one without impurity peaks. SEM images of fresh and recovered p-SiO$_2$-NH$_3$-Fe$_{11}$POM@CdS (Fig. S24) give the very similar morphology, indicating the good stability of the hybrid catalyst.

The enhanced catalytic performance over p-SiO$_2$-NH$_3$-Fe$_{11}$POM@CdS for H$_2$ evolution may be ascribed to the following reasons: (i) Enrichment effect of p-SiO$_2$-NH$_2$@CdS to Fe$_{11}$POM due to electrostatic interaction between p-SiO$_2$-NH$_3^+$ and Fe$_{11}$POM. (ii) Confinement Fe$_{11}$POM into p-SiO$_2$-NH$_2$@CdS interstitial space prevents Fe$_{11}$POM desorption. (iii) Under light irradiation (λ = 420 nm), in situ photogenerated holes and electrons directionally flow inward and outward of p-SiO$_2$-NH$_2$@CdS interstitial space, which promotes charge separation and then makes electrons accumulated in Fe$_{11}$POM for H$_2$ evolution.

3.3. Exploration of electron transfer direction and Fe^{2+} intermediate species

Photoelectrochemical measurements were carried out to illustrate the ability of photo-induced charge separation [53]. The transient photocurrent-time (i-t) curves of p-SiO$_2$-NH$_2$@CdS, Fe$_{11}$POM and p-SiO$_2$-NH$_3$-Fe$_{11}$POM@CdS samples are presented for each light on and off event in multiple 30 s cycles (Fig. 5a). The p-SiO$_2$-NH$_3$-Fe$_{11}$POM@CdS composite exhibits highest photocurrent density due to the introduction of Fe$_{11}$POM catalyst, which promotes efficient charge separation, impedes recombination of photoexcited electrons and holes, and enhances light absorption. Additionally, the smallest semicircle in electrochemical impedance spectroscopy (EIS) Nyquist plot of p-SiO$_2$-NH$_3$-Fe$_{11}$POM@CdS (Fig. 5b) among all as-prepared photoanodes once again signifies the most effective separation of the photo-induced charge carriers and fastest interfacial charge transfer [56, 57].

The steady-state photoluminescence (PL) spectra were conducted to probe the recombination efficiency of photoinduced electrons and holes (Fig. 5c) [58,59]. The PL intensity of p-SiO$_2$-NH$_3$-Fe$_{11}$POM@CdS has a distinct weakening compared to that of p-SiO$_2$-NH$_2$@CdS, manifesting the recombination of light excited electrons and holes is more effectively prohibited. The above results elucidate the improved separation and migration of photogenerated charge carriers over p-SiO$_2$-NH$_3$-Fe$_{11}$POM@CdS, which leads to good H$_2$ evolution performance.

As shown in Fig. 5d-f, kelvin probe force microscopy (KPFM) and surface photovoltage (SPV) measurements over p-SiO$_2$-NH$_3$-
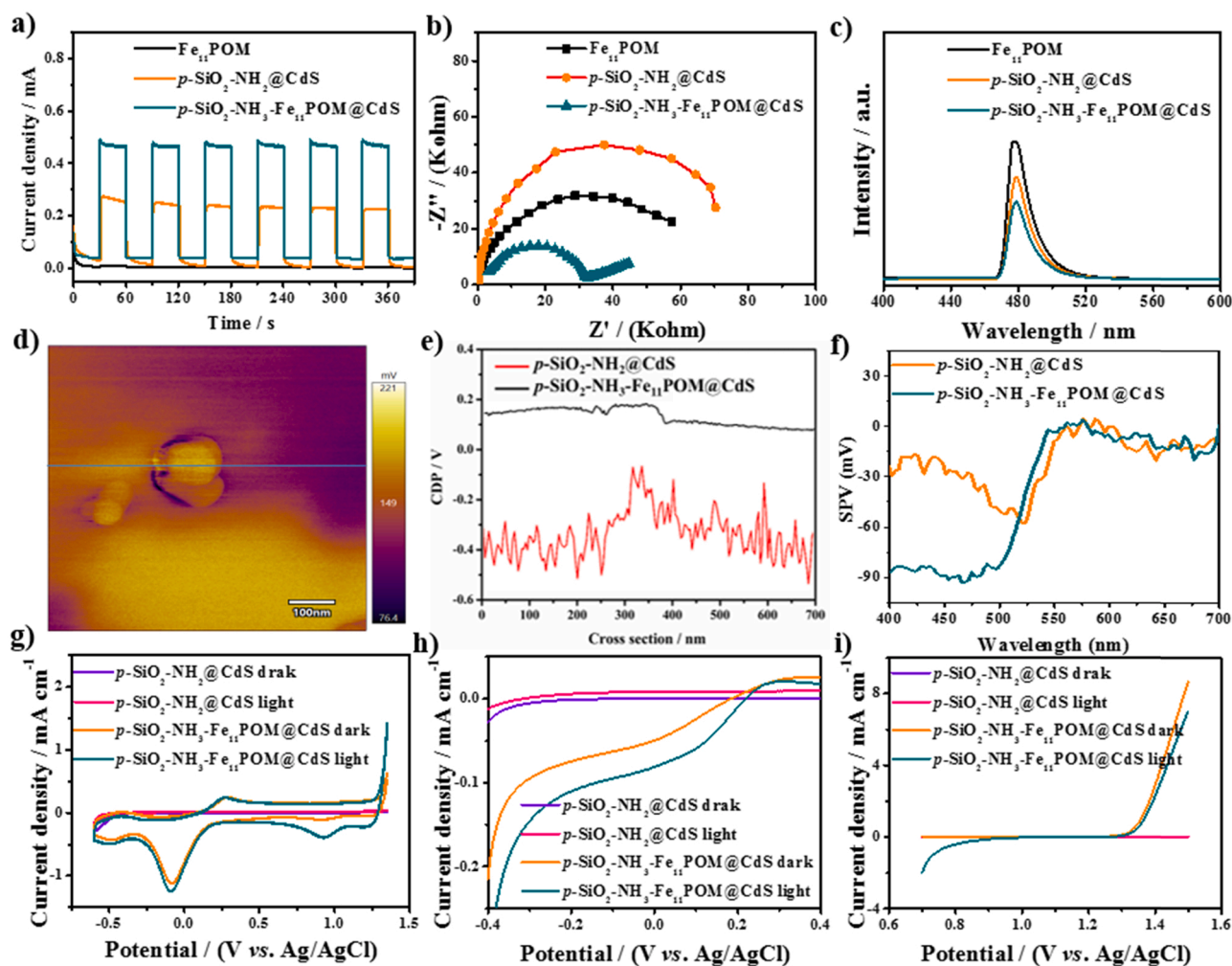
Fig. 5. The test over p-SiO$_2$-NH$_2$@CdS, Fe$_{11}$POM and p-SiO$_2$-NH$_3$-Fe$_{11}$POM@CdS samples: (a) The transient photocurrent response and (b) Nyquist plots of EIS with a three-electrode system. (c) The room-temperature PL emission spectra. (d) AFM image of p-SiO$_2$-NH$_3$-Fe$_{11}$POM@CdS. (e) KPFM of p-SiO$_2$-NH$_2$@CdS and p-SiO$_2$-NH$_3$-Fe$_{11}$POM@CdS. (f) Spatially resolved SPV amplitude spectra at the nanoscale level. The electrochemical measurements of p-SiO$_2$-NH$_2$@CdS and p-SiO$_2$-NH$_3$-Fe$_{11}$POM@CdS samples under dark and light illumination: (g) CV curves; (h) Current vs. potential profiles for the H$_2$ evolution reaction; (i) Current vs. potential profiles for the O$_2$ evolution reaction.

Fe$_{11}$POM@CdS hybrid catalyst were carried out to explore the separation and transfer behaviors of the photo-excited charge carriers. From the perspective of numerical value of the scale bar, the surface potential increases from $-$ 83 to 180 mV after Fe$_{11}$POM introduction, meaning p-SiO$_2$-NH$_3$-Fe$_{11}$POM@CdS has an upward band bending in the space charge region (Fig. 5e). Before the p-SiO$_2$-NH$_3$-Fe$_{11}$POM@CdS catalyst is formed, Fe$_{11}$POM is negative charge, and p-SiO$_2$-NH$_2$@CdS holds positive charge. The redistributed charges lead to the potential increased across the space charge region and enhance the surface potentials [60]. After introduction of Fe$_{11}$POM, the surface potential is more positive and free holes migrate to the surface. The captured holes improve the separation efficiency of photogenerated electrons and holes on surface. A small SPV value over p-SiO$_2$-NH$_2$@CdS was detected due to the poor electron-hole separation efficiency (Fig. 5f). For hybrid catalyst of p-SiO$_2$-NH$_3$-Fe$_{11}$POM@CdS, the introduction of Fe$_{11}$POM shows more negative signals for electron transfer direction from p-SiO$_2$-NH$_2$@CdS to Fe$_{11}$POM.

To confirm the formation of intermediate species of Fe^{2+} during the photocatalytic process, following experiments were executed. In Fig. 5g, the CVs of p-SiO$_2$-NH$_3$-Fe$_{11}$POM@CdS show obviously redox peaks compared to that of p-SiO$_2$-NH$_2$@CdS, manifesting the catalytic activity of p-SiO$_2$-NH$_3$-Fe$_{11}$POM@CdS is enhanced after the introduction of Fe$_{11}$POM. The characteristic peaks of p-SiO$_2$-NH$_3$-Fe$_{11}$POM@CdS

located at $\sim$0.93 and $\sim$1.22 V manifest two larger values under light irradiation than those of in the dark. From Fig. 5h, it can be seen that p-SiO$_2$-NH$_3$-Fe$_{11}$POM@CdS has a more positive redox peak under light irradiation than those of in the dark (0.09 vs. $-$0.01 V against Ag/AgCl). This redox peak is associated with the conversion from Fe^{3+} to Fe^{2+}, and the light irradiation promotes a positive shift of 0.1 V for p-SiO$_2$-NH$_3$-Fe$_{11}$POM@CdS.

No oxidation peak of p-SiO$_2$-NH$_3$-Fe$_{11}$POM@CdS is observed for the O$_2$ evolution reaction, and this curve is weakened upon light irradiation (Fig. 5i). As shown in Fig. S25, the produced Fe^{2+} species is detected by K$_3$[Fe(CN)$_6$] with a blue-green precipitate KFe[Fe(CN)$_6$] by Tengs blue color reaction. Similar phenomenon is not observed in the control experiment with p-SiO$_2$-NH$_2$@CdS under the same test conditions. Based on the above analysis, the formation of Fe^{2+} intermediate species is essential for the photocatalytic H$_2$ evolution over p-SiO$_2$-NH$_3$-Fe$_{11}$POM@CdS catalyst.

3.4. Mechanistic insight of photocatalytic process

As shown in Fig. S26a, the sample before photoactivation shows an absorbance at excitation band of 508 nm and the characteristic absorbance is observed at 230 and 277 nm. The sample after photoactivation exhibits very strong absorption in the whole range. The rate of H$_2$

evolution rapidly increases in the first 12 min of light irradiation and remains nearly constant afterwards (Fig. S26b). This timescale of activation of the H_2 evolution rate (~12 min) matches well with that of the color change of p-SiO$_2$-NH$_3$-Fe$_{11}$POM@CdS during the catalytic process (Fig. S27).

An interesting photochromic phenomenon is observed during the catalytic process of p-SiO$_2$-NH$_3$-Fe$_{11}$POM@CdS (Fig. S27). The color of the reaction solution changes from yellow to claybank, then to brown green under visible light irradiation. The solution was deaerated by purging with Ar gas for 30 min before reaction. The brown green solution retains its color even after the light is turned off with the rubber stopper tightly closed. When the brown green of the reaction suspension was exposed in air, the color changes back to yellow within 2 min, in which a photoactivation process is finished. However, similar phenomenon is not observed in the control experiment with p-SiO$_2$-NH$_2$@CdS under the same test conditions.

The above experimental observations are conducive to elucidate the mechanism of H_2 evolution for the spatially separated system of p-SiO$_2$-

NH$_3$-Fe$_{11}$POM@CdS (Fig. 6). In the catalyst assembly, Fe$_{11}$POM acts as catalyst and p-SiO$_2$-NH$_2$@CdS acts as light-harvesting material as well as Fe$_{11}$POM enrichment center, respectively. Initially, the p-SiO$_2$-NH$_3$-Fe$_{11}$POM@CdS catalyst is in a state of inactivity (Fig. 6a). After absorbing light of p-SiO$_2$-NH$_2$@CdS, the electrons and holes generated on p-SiO$_2$-NH$_2$@CdS interstitial space flow inward and outward, respectively. The state of p-SiO$_2$-NH$_3$-Fe$_{11}$POM@CdS changes from inactive to photoexcited (intermediate state I). The gathered holes at the outside surface of p-SiO$_2$-NH$_2$@CdS are used for proton formation via oxidative reforming of the sacrificial reagent of lactic acid (Fig. 6b). While, the accumulated electrons enter into p-SiO$_2$-NH$_2$@CdS interstitial space, then migrate to Fe$_{11}$POM (intermediate state II).

Furthermore, the enriched electrons at Fe$_{11}$POM are responsible for H^+ reduction to H_2 generation (active state). In this process, Fe^{3+} in Fe$_{11}$POM is reduced to Fe^{2+} active species whereas lactic acid acts as an electron donor. The existence of Fe^{2+} intermidiate species in p-SiO$_2$-NH$_3$-Fe$_{11}$POM@CdS answers for the color change in N_2 atmosphere under visible light irradiation, which is all-important for the

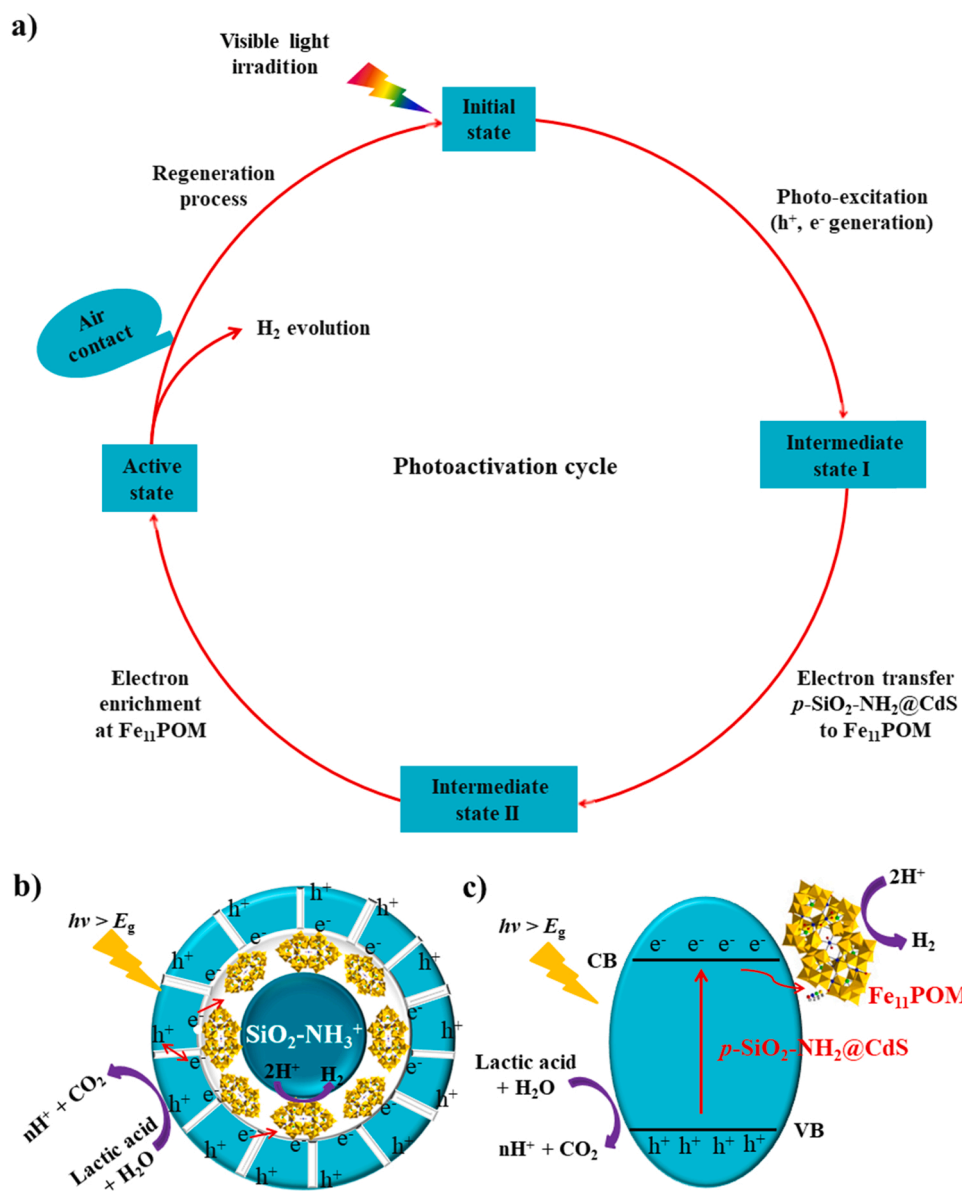**Fig. 6.** (a) The photoactivation cycle over p-SiO$_2$-NH$_3$-Fe$_{11}$POM@CdS for photocatalytic H_2 evolution under visible light irradiation. (b) Mechanism of photogenerated charge separation over p-SiO$_2$-NH$_3$-Fe$_{11}$POM@CdS. (c) Charge transfer schematic diagram of the spatially separated system over p-SiO$_2$-NH$_3$-Fe$_{11}$POM@CdS.

photocatalytic H_2 evolution over p-SiO$_2$-NH$_3$-Fe$_{11}$POM@CdS catalyst. Finally, the active state is easily recovered to its initial inactive state by regeneration process when the hybrid catalyst is simply exposed to air for 2 min.

4. Conclusion

In summary, we have successfully prepared a p-SiO$_2$-NH$_3$-Fe$_{11}$POM@CdS photocatalyst assembly for H_2 evolution by confining Fe$_{11}$POM molecular catalyst in p-SiO$_2$-NH$_2$@CdS interstitial space, which realizes "homogenous in heterogeneous catalysis". In the hybrid catalyst, Fe$_{11}$POM acts as catalyst and p-SiO$_2$-NH$_3$@CdS acts as light-harvesting material as well as Fe$_{11}$POM enrichment center due to electrostatic interaction between p-SiO$_2$-NH$_3^+$ and Fe$_{11}$POM. In the presence of lactic acid as sacrificial reagent under visible light irradiation ($\lambda = 420$ nm), p-SiO$_2$-NH$_3$-Fe$_{11}$POM@CdS exhibits high photocatalytic H_2 evolution activity of 23.1 mmol g^{-1} h^{-1} with TON of 3225 and AQE of ~71%, and its H_2 evolution rate is 10.1 times higher than that of p-SiO$_2$-NH$_2$@CdS. Upon generation from p-SiO$_2$-NH$_2$@CdS, holes and electrons directionally flow inward and outward of the p-SiO$_2$-NH$_2$@CdS interstitial space. The electrons transfer from p-SiO$_2$-NH$_2$@CdS to Fe$_{11}$POM, making electrons accumulated in Fe$_{11}$POM for H_2 evolution. The result shows p-SiO$_2$-NH$_3$-Fe$_{11}$POM@CdS hybrid catalyst significantly improves charge separation and inhibit the recombination of holes and electrons. In photocatalytic process, the formation of Fe^{2+} intermediate as the active species is found, which is associated with photochromic phenomenon. This work stimulates the study on the rational design of efficient catalysts by coupling POMs and functional semiconductor with well-defined structure for the utilization of solar energy with relevant chemical reactions.

CRediT authorship contribution statement

Yinjuan Dong prepared, characterized, tested the catalysts and wrote the paper. Bonan Li offered a help for drawing schematic illustration. Xiaohu Li and Meiyu Zhang provided a help for photoeletrochemical measurements. Qiyu Hu, Mengxue Chen, Yu Feng revised the first manuscript. Yong Ding supervised the project and wrote the paper.

Declaration of Competing Interest

The authors declare that they have no known competing financial interests or personal relationships that could have appeared to influence the work reported in this paper.

Acknowledgements

Appendix A. Supporting information

Supplementary data associated with this article can be found in the online version at doi:10.1016/j.apcatb.2021.120998.

References

[1] H. Tong, S.X. Ouyang, Y.P. Bi, N. Umezawa, M. Oshikiri, J.H. Ye, Nano-photocatalytic materials: possibilities and challenges, Adv. Mater. 24 (2012) 229–251.

[2] M.F. Kuehnel, K.L. Orchard, K.E. Dalle, E. Reisner, Selective photocatalytic CO$_2$ reduction in water through anchoring of a molecular Ni catalyst on CdS nanocrystals, J. Am. Chem. Soc. 139 (2017) 7217–7223.

[3] T.A. Kandiel, I. Ivanova, D.W. Bahnemann, Long-term investigation of the photocatalytic hydrogen production on platinized TiO$_2$: an isotopic study, Energy Environ. Sci. 7 (2014) 1420–1425.

[4] B.H. Lee, S. Park, M. Kim, A.K. Sinha1, S.C. Lee, E. Jung, W.J. Chang, K.S. Lee, J. H. Kim, S.P. Cho, H. Kim, K.T. Nam, T. Hyeon, Reversible and cooperative photoactivation of single-atom Cu/TiO$_2$ photocatalysts, Nat. Mater. 18 (2019) 620–626.

[5] H.Q. Xu, S.Z. Yang, X. Ma, J.E. Huang, H.L. Jiang, Unveiling charge-separation dynamics in CdS/metal-organic framework composites for enhanced photocatalysis, ACS Catal. 8 (2018) 11615–11621.

[6] M. Xiao, L. Zhang, B. Luo, M.Q. Lyu, Z.L. Wang, H.M. Huang, S.C. Wang, A. Du, L. Z. Wang, Molten-salt-mediated synthesis of an atomic nickel Co-catalyst on TiO$_2$ for improved photocatalytic H$_2$ evolution, Angew. Chem. Int. Ed. 59 (2020) 7230–7234.

[7] D. Wang, X.Q. Gong, Function-oriented design of robust metal cocatalyst for photocatalytic hydrogen evolution on metal/titania composites, Nat. Commun. 12 (2021) 158.

[8] S.B. Wang, Y. Wang, S.L. Zhang, S.Q. Zang, X.W. (David) Lou, Supporting ultrathin ZnIn$_2$S$_4$ nanosheets on Co/N-doped graphitic carbon nanocages for efficient photocatalytic H$_2$ generation, Adv. Mater. 31 (2019), 1903404.

[9] Q.Z. Zhang, S.Y. Huang, J.J. Deng, D.T. Gangadharan, F. Yang, Z.H. Xu, G. Giorgi, M. Palummo, M. Chaker, D.L. Ma, Ice-assisted synthesis of black phosphorus nanosheets as a metal-free photocatalyst: 2D/2D heterostructure for broadband H$_2$ evolution, Adv. Funct. Mater. 29 (2019), 1902486.

[10] S.N. Xiao, W.R. Dai, X.Y. Liu, D.L. Pan, H.J. Zou, G.S. Li, G.Q. Zhang, C.L. Su, D. Q. Zhang, W. Chen, H.X. Li, Microwave-induced metal dissolution synthesis of core–shell copper nanowires/ZnS for visible light photocatalytic H$_2$ evolution, Adv. Energy Mater. 9 (2019), 1900775.

[11] R.F. Chen, Y. Wang, Y. Ma, A. Mal, X.Y. Gao, L. Gao, L.J. Qiao, X.B. Li, L.Z. Wu, C. Wang, Rational design of isostructural 2D porphyrin-based covalent organic frameworks for tunable photocatalytic hydrogen evolution, Nat. Commun. 12 (2021) 1354.

[12] S. Ghosh, A. Nakada, M.A. Springer, T. Kawaguchi, K. Suzuki, H. Kaji, I. Baburin, A. Kuc, T. Heine, H. Suzuki, R. Abe, S. Seki, Identification of prime factors to maximize the photocatalytic hydrogen evolution of covalent organic frameworks, J. Am. Chem. Soc. 142 (2020) 9752–9762.

[13] Y.H. Pi, X.Y. Feng, Y. Song, Z.W. Xu, Z. Li, W.B. Lin, Metal-organic frameworks integrate Cu photosensitizers and secondary building unit-supported Fe catalysts for photocatalytic hydrogen evolution, J. Am. Chem. Soc. 142 (2020) 10302–10307.

[14] Z.F. Zhao, Y.L. Zheng, C. Wang, S. Zhang, J. Song, Y.F. Li, S.Q. Ma, P. Cheng, Z. J. Zhang, Y. Chen, Fabrication of robust covalent organic frameworks for enhanced visible-light-driven H2 evolution, ACS Catal. 11 (2021) 2098–2107.

[15] H. Hu, Z. Wang, L. Cao, L. Zeng, C. Zhang, W. Lin, C. Wang, Metal–organic frameworks embedded in a liposome facilitate overall photocatalytic water splitting, Nat. Chem. 13 (2021) 358–366.

[16] X.M. Liang, S.Z. Yang, J.Y. Yang, W.J. Sun, X.Y. Li, B.C. Ma, J.E. Huang, J. W. Zhang, L.L. Duan, Y. Ding, Covalent immobilization of molecular complexes on metal-organic frameworks towards robust and highly efficient hterogeneous water oxidation catalysts, Appl. Catal. B-Environ. 291 (2021), 120070.

[17] J. Li, M.F. Stephanopoulos, Y.N. Xia, Introduction: heterogeneous single-atom catalysis, Chem. Rev. 120 (2020) 11699–11702.

[18] Y. Hu, X.Q. Hao, Z.W. Cui, J. Zhou, S.Q. Chu, Y. Wang, Z.G. Zou, Enhanced photocarrier separation in conjugated polymer engineered CdS for direct Z-scheme photocatalytic hydrogen evolution, Appl. Catal. B-Environ. 260 (2020) 118131.

[19] H. Yang, C. Yang, N.N. Zhang, K.L. Mo, Q. Li, K.L. Lv, J.J. Fan, L.L. Wen, Drastic promotion of the photoreactivity of MOF ultrathin nanosheets towards hydrogen production by deposition with CdS nanorods, Appl. Catal. B-Environ. 285 (2021), 119801.

[20] Q.M. Sun, N. Wang, J.H. Yu, J.C. Yu, A hollow porous CdS photocatalyst, Adv. Mater. 30 (2018), 1804368.

[21] X.J. She, J.J. Wu, H. Xu, J. Zhong, Y. Wang, Y.H. Song, K.Q. Nie, Y. Liu, Y.C. Yang, M.F. Rodrigues, R. Vajtai, J. Lou, D.L. Du, H.M. Li, P.M. Ajayan, High efficiency photocatalytic water splitting using 2D α-Fe$_2$O$_3$/g-C$_3$N$_4$ Z-scheme catalysts, Adv. Energy Mater. 31 (2017), 1700025.

[22] T. Xiong, W.L. Cen, Y.X. Zhang, F. Dong, Bridging the g-C$_3$N$_4$ interlayers for enhanced photocatalysis, ACS Catal. 6 (2016) 2462–2472.

[23] X.J. Chen, R. Shi, Q. Chen, Z.J. Zhang, W.J. Jiang, Y.F. Zhu, T.R. Zhang, Three-dimensional porous g-C$_3$N$_4$ for highly efficient photocatalytic overall water splitting, Nano Energy 59 (2019) 644–650.

[24] W.N. Xing, W.G. Tu, Z.H. Han, Y.D. Hu, Q.Q. Meng, G. Chen, Template-induced high-crystalline g-C$_3$N$_4$ nanosheets for enhanced photocatalytic H$_2$ evolution, ACS Energy Lett. 3 (2018) 514–519.

[25] Y. Jiang, H.Y. Ning, C.G. Tian, B.J. Jiang, Q. Li, H.J. Yan, X.L. Zhang, J.Q. Wang, L. Q. Jing, H.G. Fu, Single-crystal TiO$_2$ nanorods assembly for efficient and stable cocatalyst-free photocatalytic hydrogen evolution, Appl. Catal. B-Environ. 229 (2018) 1–7.

[26] H.L. Xiong, L.L. Wu, Y. Liu, T. Gao, K.Q. Li, Y. Long, R. Zhang, L. Zhang, Z.A. Qiao, Q.S. Huo, X. Ge, S.Y. Song, H.J. Zhang, Controllable synthesis of mesoporous TiO$_2$ polymorphs with tunable crystal structure for enhanced photocatalytic H$_2$ production, Adv. Energy Mater. 9 (2019), 1901634.

[27] L.M. Sun, Y.S. Yuan, F. Wang, Y.L. Zhao, W.W. Zhan, X.G. Han, Selective wet-chemical etching to create TiO$_2$@MOF frame heterostructure for efficient photocatalytic hydrogen evolution, Nano Energy 74 (2020), 104909.

[28] R.G. Li, H.X. Han, F.X. Zhang, D. Wang, C. Li, Highly efficient photocatalysts constructed by rational assembly of dual-cocatalysts separately on different facets of BiVO$_4$, Energy Environ. Sci. 7 (2014) 1369–1376.

[29] K. Fuku, R. Takioka, K. Iwamura, M. Todoroki, K. Sayama, N. Ikenaga, Photocatalytic H$_2$O$_2$ production from O$_2$ under visible light irradiation over

phosphate ion-coated Pd nanoparticles-supported BiVO$_4$, Appl. Catal. B-Environ. 272 (2020), 119003.

[30] J.M. Wang, L. Xu, T.X. Wang, R.J. Li, Y.X. Zhang, J. Zhang, T.Y. Peng, Porphyrin conjugated polymer grafted onto BiVO$_4$ nanosheets for efficient Z-scheme overall water splitting via cascade charge transfer and single-atom catalytic sites, Adv. Energy Mater. 11 (2021), 2003575.

[31] Y.J. Dong, Q. Han, Q.Y. Hu, C.J. Xu, C.Z. Dong, Y. Peng, Y. Ding, Y.Q. Lan, Carbon quantum dots enriching molecular nickel polyoxometalate over CdS semiconductor for photocatalytic water splitting, Appl. Catal. B-Environ. 293 (2021), 120214.

[32] Z.Z. Ai, G. Zhao, Y.Y. Zhong, Y.L. Shao, B.B. Huang, Y.Z. Wu, X.P. Hao, Phase junction CdS: high efficient and stable photocatalyst for hydrogen generation, Appl. Catal. B-Environ. 221 (2018) 179–186.

[33] C. Zhu, C.G. Liu, Y.J. Zhou, Y.J. Fu, S.J. Guo, H. Li, S.Q. Zhao, H. Huang, Y. Liu, Z. H. Kang, Carbon dots enhance the stability of CdS for visible-light-driven overall water splitting, Appl. Catal. B-Environ. 216 (2017) 114–121.

[34] Z.Q. Jiang, J.X. Liu, M.Y. Gao, X. Fan, L. Zhang, J. Zhang, Assembling polyoxo-titanium clusters and CdS nanoparticles to a porous matrix for efficient and tunable H$_2$-evolution activities with visible light, Adv. Mater. 29 (2017), 1603369.

[35] Q. Li, B.D. Guo, J.G. Yu, J.R. Ran, B.H. Zhang, H.J. Yan, J.R. Gong, Highly efficient visible-light-driven photocatalytic hydrogen production of CdS-cluster-decorated graphene nanosheets, J. Am. Chem. Soc. 133 (2011) 10878–10884.

[36] M.Y. Xing, B.C. Qiu, M.M. Du, Q.H. Zhu, L.Z. Wang, J.L. Zhang, Spatially separated CdS shells exposed with reduction surfaces for enhancing photocatalytic hydrogen evolution, Adv. Funct. Mater. 27 (2017), 1702624.

[37] Z.J. Han, F. Qiu, R. Eisenberg, P.L. Holland, T.D. Krauss, Robust photogeneration of H$_2$ in water using semiconductor nanocrystals and a nickel catalyst, Science 338 (2012) 1321–1324.

[38] R. Chen, Z.H. Yan, X.J. Kong, L.S. Long, L.S. Zheng, Integration of lanthanide–transition-metal clusters onto CdS surfaces for photocatalytic hydrogen evolution, Angew. Chem. Int. Ed. 57 (2018) 16796–16800.

[39] G. Izzet, B. Abecassis, D. Brouri, M. Piot, B. Matt, S.A. Serapian, C. Bo, A. Proust, Hierarchical self-assembly of polyoxometalate-based hybrids driven by metal coordination and electrostatic interactions: from discrete supramolecular species to dense monodisperse nanoparticles, J. Am. Chem. Soc. 138 (2016) 5093–5099.

[40] B. Chakraborty, G. Gan-Or, Y. Duan, M. Raula, I.A. Weinstock, Visible-light-driven water oxidation with a polyoxometalate complexed hematite core of 275 iron atoms, Angew. Chem. Int. Ed. 131 (2019) 6656–6661.

[41] B. Chakraborty, G. Gan-Or, Y. Duan, M. Raula, I.A. Weinstock, Visible-light-driven water oxidation with a polyoxometalate complexed hematite core of 275 iron atoms, Angew. Chem. Int. Ed. 58 (2019) 6584–6589.

[42] X.Q. Du, J.L. Zhao, J.Q. Mi, Y. Ding, P.P. Zhou, B.C. Ma, J.W. Zhao, J. Song, Efficient photocatalytic H$_2$ evolution catalyzed by an unprecedented robust molecular semiconductor {Fe$_{11}$} nanocluster without cocatalysts at neutral conditions, Nano Energy 16 (2015) 247–255.

[43] H.J. Lv, W.W. Guo, K.F. Wu, Z.Y. Chen, J. Bacsa, D.G. Musaev, Y.R.V. Geletii, S. M. Lauinger, T.Q. Lian, C.L. Hill, A noble-metal-free, tetra-nickel polyoxotungstate catalyst for efficient photocatalytic hydrogen evolution, J. Am. Chem. Soc. 136 (2014) 14015–14018.

[44] F.Y. Song, Y. Ding, B.C. Ma, C.M. Wang, Q. Wang, X.Q. Du, S. Fu, J. Song, K$_7$[Co^{III}Co^{II}(H$_2$O)W$_{11}$O$_{39}$]: a molecular mixed-valence keggin polyoxometalate catalyst of high stability and efficiency for visible light-driven water oxidation, Energy Environ. Sci. 6 (2013) 1170–1184.

[45] Q.S. Yin, J.M. Tan, C. Besson, Y.V. Geletii, D.G. Musaev, A.E. Kuznetsov, Z. Luo, K. I. Hardcastle, C.L. Hill, A fast soluble carbon-free molecular water oxidation catalyst based on abundant metals, Sciense 328 (2010), 342–328.

[46] L. Yang, J. Zhao, J.W. Zhao, J.Y. Niu, Syntheses, crystal structures, and magnetic properties of the banana-shaped tungstophosphates: [M$_6$(H$_2$O)$_2$(PW9O$_{34}$)$_2$(PW$_6$O$_{26}$)]$^{17-}$ (M^{II}=Ni^{II}, Co^{II}), J. Coord. Chem. 65 (2012) 3363–3371.

[47] J. Wei, Y.Y. Feng, P.P. Zhou, Y. Liu, J.Y. Xu, R. Xiang, Y. Ding, C.C. Zhao, L.Y. Fan, C.W. Hu, A bioinspired molecular polyoxometalate catalyst with two cobalt(II) oxide cores for photocatalytic water oxidation, ChemSusChem 8 (2015) 2630–2634.

[48] X.B. Han, Y.G. Li, Z.M. Zhang, H.Q. Tan, Y. Lu, E.B. Wang, Polyoxometalate-based nickel clusters as visible light-driven water oxidation catalysts, J. Am. Chem. Soc. 137 (2015) 5486–5493.

[49] X.B. Han, Z.M. Zhang, T. Zhang, Y.G. Li, W.B. Lin, W. You, Z.M. Su, E.B. Wang, Polyoxometalate-based cobalt-phosphate molecular catalysts for visible light-driven water oxidation, J. Am. Chem. Soc. 136 (2014) 5359–5366.

[50] S. Yasuhiro, K. Yusuke, S. Hirokatsu, T. Shunsuke, I. Satoshi, H. Takayuki, Effects of surface defects on photocatalytic H$_2$O$_2$ production by mesoporous graphitic carbon nitride under visible light irradiation, ACS Catal. 5 (2015) 3058–3066.

[51] X.M. Ning, Y.L. Wu, X.F. Ma, Z. Zhang, R.Q. Gao, J. Chen, D.L. Shan, X.Q. Lu, A novel charge transfer channel to simultaneously enhance photocatalytic water splitting activity and stability of CdS, Adv. Funct. Mater. 29 (2019), 1902992.

[52] X.Z. Yue, S.S. Yi, R.W. Wang, Z.T. Zhang, S.L. Qiu, Cobalt phosphide modified titanium oxide nanophotocatalysts with significantly enhanced photocatalytic hydrogen evolution from water splitting, Small 13 (2017), 1603301.

[53] X.Q. Hao, Y. Hu, Z.W. Cui, J. Zhou, Y. Wang, Z.G. Zou, Self-constructed facet junctions on hexagonal CdS single crystals with high photoactivity and photostability for water splitting, Appl. Catal. B-Environ. 244 (2019) 694–703.

[54] S.S. Yi, J.M. Yan, B.R. Wulan, S.J. Li, K.H. Liu, Q. Jiang, Noble-metal-free cobalt phosphide modified carbon nitride: an efficient photocatalyst for hydrogen generation, Appl. Catal. B-Environ. 200 (2017) 477–483.

[55] Z.H. Chen, W.L. Wang, Z.G. Zhang, X.M. Fang, High-efficiency visible-light-driven Ag$_3$PO$_4$/AgI photocatalysts: Z-scheme photocatalytic mechanism for their enhanced photocatalytic activity, J. Phys. Chem. C. 117 (2013) 19346–19352.

[56] S. Ye, C.M. Ding, R.T. Chen, F.T. Fan, P. Fu, H. Yin, X.L. Wang, Z.L. Wang, P.W. Du, C. Li, Mimicking the key functions of photosystem II in artificial photosynthesis for photoelectrocatalytic water splitting, J. Am. Chem. Soc. 140 (2018) 3250–3256.

[57] F.R. Cao, L.X. Meng, M. Wang, W. Tian, L. Li, Gradient energy band driven high-performance self-powered perovskite/CdS photodetector, Adv. Mater. 31 (2019), 1806725.

[58] J.K. Zhang, Z.B. Yu, Z. Gao, H.B. Ge, S.C. Zhao, C.Q. Chen, S.A. Chen, X.L. Tong, M. H. Wang, Z.F. Zheng, Y. Qin, Porous TiO$_2$ nanotubes with spatially separated platinum and CoO$_x$ cocatalysts produced by atomic layer deposition for photocatalytic hydrogen production, Angew. Chem. Int. Ed. 56 (2017) 816–820.

[59] R. Chen, Z.H. Yan, X.J. Kong, L.S. Long, L.S. Zheng, Integration of lanthanide–transition–metal clusters onto CdS surfaces for photocatalytic hydrogen evolution, Angew. Chem. Int. Ed. 57 (2018) 16796–16800.

[60] J. Zhu, F.T. Fan, R.T. Chen, H.Y. An, Z.C. Feng, C. Li, Direct imaging of highly anisotropic photogenerated charge separations on different facets of a single BiVO$_4$ photocatalyst, Angew. Chem. Int. Ed. 54 (2015) 9111–9114.